nature geoscience

LETTERS

PUBLISHED ONLINE: 6 AUGUST 2015 | DOI: 10.1038/NGEO2518

Lower edge of locked Main Himalayan Thrust unzipped by the 2015 Gorkha earthquake

Jean-Philippe Avouac[1]*, Lingsen Meng[2], Shengji Wei[3], Teng Wang[4] and Jean-Paul Ampuero[5]

Large earthquakes are thought to release strain on previously locked faults. However, the details of how earthquakes are initiated, grow and terminate in relation to pre-seismically locked and creeping patches is unclear[1–4]. The 2015 M_w 7.8 Gorkha, Nepal earthquake occurred close to Kathmandu in a region where the prior pattern of fault locking is well documented[5]. Here we analyse this event using seismological records measured at teleseismic distances and Synthetic Aperture Radar imagery. We show that the earthquake originated northwest of Kathmandu within a cluster of background seismicity that fringes the bottom of the locked portion of the Main Himalayan Thrust fault (MHT). The rupture propagated eastwards for about 140 km, unzipping the lower edge of the locked portion of the fault. High-frequency seismic waves radiated continuously as the slip pulse propagated at about 2.8 km s^{-1} along this zone of presumably high and heterogeneous pre-seismic stress at the seismic–aseismic transition. Eastward unzipping of the fault resumed during the M_w 7.3 aftershock on 12 May. The transfer of stress to neighbouring regions during the Gorkha earthquake should facilitate future rupture of the areas of the MHT adjacent and updip of the Gorkha earthquake rupture.

On 25 April 2015, an earthquake with moment magnitude M_w 7.8 occurred along the Himalayan front close to Kathmandu (Fig. 1). The epicentre was located 80 km to the west–northwest of Kathmandu within a long-identified zone of clustered seismicity that runs beneath the front of the high Himalaya[6]. The focal mechanism[7] indicating thrusting on a subhorizontal fault dipping about 10° northwards and the 15 km hypocentral depth[7] make it likely that this earthquake ruptured the MHT, the main fault along which northern India underthrusts the Himalaya at a rate of approximately 2 cm yr^{-1} (ref. 8). A M_w 7.3 aftershock with a very similar focal mechanism[9] occurred on 12 May, 75 km east of Kathmandu (Fig. 1). The geometry of the MHT in the hypocentral area is relatively well known from various geophysical experiments[10,11]. Geodetic measurements collected over the past 20 years revealed that this fault has remained locked over this time period[5,12] and the pattern of locking is now well constrained[5] (Fig. 1), allowing a detailed comparison with the rupture process during the Gorkha earthquake.

We imaged the rupture process by back-projecting[13] teleseismic P-waves recorded by the Australian seismic network (Fig. 2a and Supplementary Fig. 1) using the Multitaper-MUSIC array processing technique. The technique tracks the spatio-temporal evolution of the sources of high-frequency radiation (0.5–2 Hz) during the rupture process (Supplementary Fig. 2; see Methods). The back-projection forms coherent sources for about 60 s after initiation of the rupture. The high-frequency sources are almost linearly distributed for about 45 s, and their timing indicates a 2.72 ± 0.13 km s^{-1} eastward propagation (Fig. 2b). They follow remarkably well the downdip edge of the locked zone (Fig. 1) and the cluster of background seismicity (Fig. 2a), including a local kink northwest of Kathmandu. The amplitude rises sharply from 10 to 20 s, peaks from 20 to 40 s, and decays abruptly after about 45 s (Fig. 2c). High-frequency radiation persists after 45 s, but migrates updip in a southeastward direction. The 12 May aftershock occurred a few tens of kilometres east of where the initial phase of along-strike propagation of the rupture stopped (Fig. 2a).

We also determined a finite source model of the rupture from the joint inversion[14] of teleseismic waveforms in the 0.01–1 Hz frequency band and static surface displacements measured from SAR image offsets. The fault is assumed planar and its dip angle was adjusted to 7° by trial and error. The model assumes that, once initiated, slip accrues over a certain duration (rise time) in the wake of the rupture front. The inversion solves for the final slip amplitude, rake, rise time and rupture front velocity at each grid point (see Methods). The source model is determined so as to best fit the static surface displacements (Supplementary Fig. 3) and teleseismic waveforms (Supplementary Fig. 4). The static surface displacements were measured using two pairs of European Space Agency's Sentinel-1 radar images acquired on 17 and 29 April, and 9 April and 3 May. We ignored the possibility of post-seismic deformation over the four and eight days following the event (see Methods). The finite source model (Fig. 2) shows that the rupture propagated eastwards at 3.0 ± 0.5 km s^{-1} on average (Supplementary Fig. 5). The slip area is about 120 km in length along strike and 50 km in width along dip. The implied moment tensor is nearly identical to the W-phase moment tensor (Fig. 1). Altogether the earthquake released a total moment of 7.2×10^{20} N m, corresponding to M_w 7.84. The moment rate function shows a simple rupture with a single major pulse of 50 s duration (Fig. 2c). The 12 May aftershock falls in a gap of relatively low slip at the eastward termination of the mainshock.

The results from the back-projection and finite source inversion are in remarkable agreement during the first 45 s of the rupture. The moment release rate and the power of the high-frequency sources show the same temporal pattern (Fig. 2c). Both source imaging techniques reveal a unilateral pulse-like rupture with a narrow strip of active slip, 20–30 km wide along strike, propagating eastwards at about 2.7 to 3.0 km s^{-1} (Fig. 3 and Supplementary Animation).

[1]Bullard Laboratories, Department of Earth Sciences, University of Cambridge, Madingley Road, Cambridge CB3 0EZ, UK. [2]Department of Earth, Planetary and Space Sciences, University of California, Los Angeles, 595 Charles Young Drive East, Box 951567, Los Angeles, California 950095, USA. [3]Earth Observatory of Singapore, Nanyang Technological University, N2-01A-108, 50 Nanyang Avenue, Singapore 639798, Singapore. [4]Huffington Department of Earth Sciences, Southern Methodist University, PO Box 750395, Dallas, Texas 75275-0395, USA. [5]Seismological Laboratory, Geology and Planetary Science Division, California Institute of Technology, 1200 E. California Boulevard, Pasadena, California 91125, USA. *e-mail: avouac@gps.caltech.edu

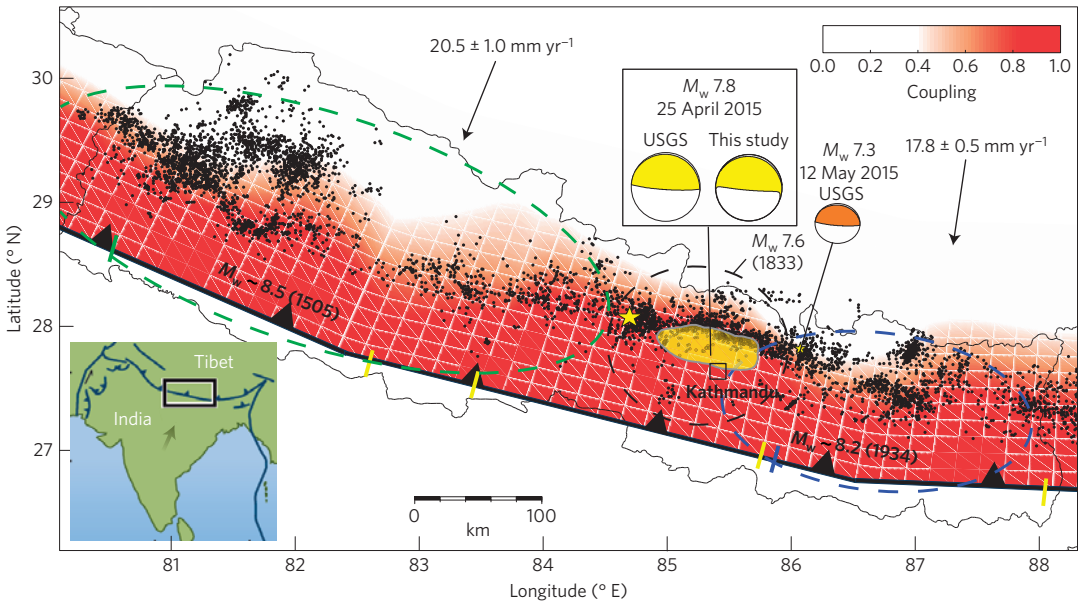

Figure 1 | Seismotectonic context of the 2015 M_w 7.8 Gorkha earthquake. Yellow patch shows area with >1 m coseismic slip. Epicentre (star), centroid location and W-phase moment tensors from USGS (refs 7,9). Interseismic coupling and convergence rate across the Himalaya from ref. 5. Dots show 1995–2003 relocated seismicity[30]. $M_w > 7.5$ historical events since 1505 (refs 18–20,23) are estimated to have occurred within the dashed ellipses, with short lines showing locations of documented surface rupture, in 1934 (blue) and 1505 (green) respectively[24,29]. Yellow short lines indicate surface ruptures more probably related to older events (possibly in 1255 AD; refs 18,24). Inset: map location and motion of India relative to Eurasia.

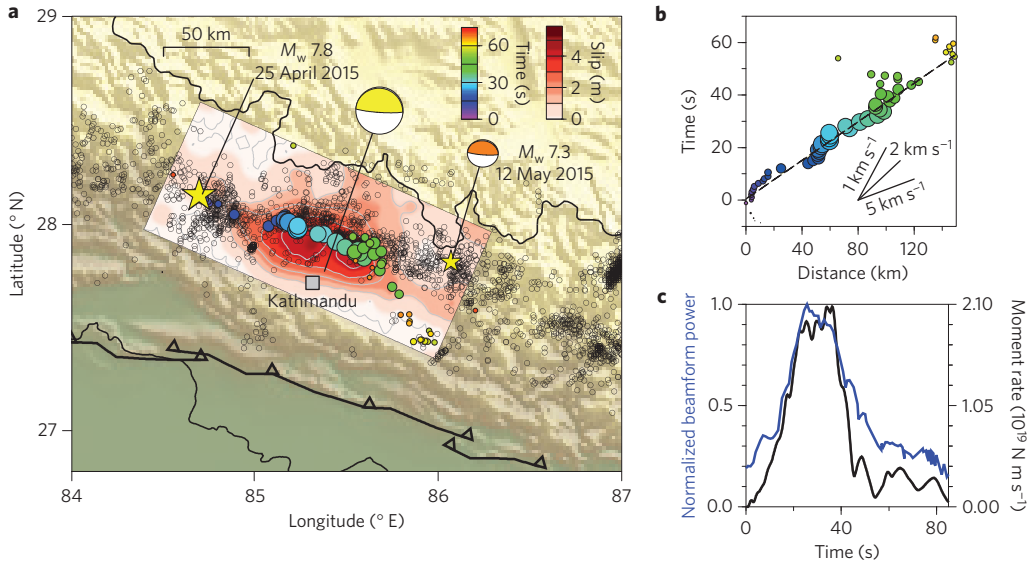

Figure 2 | Seismic rupture kinematics. a, Coseismic slip determined from joint inversion of teleseismic waveforms and SAR measurements (red shading) and locations of high-frequency (0.5–2 Hz) sources determined from back-projection of teleseismic waves (dots). Dot size is proportional to the beamforming amplitude and colour indicates the time of each window centre relative to hypocentral time. Open circles show relocated background 1995–2003 seismicity[30]. **b**, Timing of high-frequency sources as a function of distance along strike. Least squares linear regression (dashed line) indicates a rupture speed of 2.72 ± 0.13 km s^{-1}. **c**, Relative beamforming power (blue) and moment release rate from finite source inversion (black).

Contrary to the back-projection, the finite source model yields a rupture velocity that is sensitive to the epicentral location, which can be off by more than 10 km. Given the various possible sources of errors, we estimate that the two analyses agree within uncertainties and indicate a rupture velocity of 2.8 ± 0.3 km s^{-1}.

Because the finite source inversion assumes a rupture front expanding from the epicentre and because the teleseismic waveforms constrain only the moment rate function robustly, the slip distribution for each time interval is smeared along the quasi-circular isochrons of the rupture front (Fig. 3). The SAR data help limit this smearing effect by forcing the cumulative slip distribution to match the west–east trending narrow zone of surface deformation along the rupture-propagation pathway (Supplementary Fig. 3). The northern edge of the high-slip area correlates with the location of the high-frequency sources and with the edge of the locked zone (Fig. 2a). After 45 s the source model is less well constrained because of the lower signal-to-noise ratio, and the pulse becomes increasingly diffuse and smeared along isochrons.

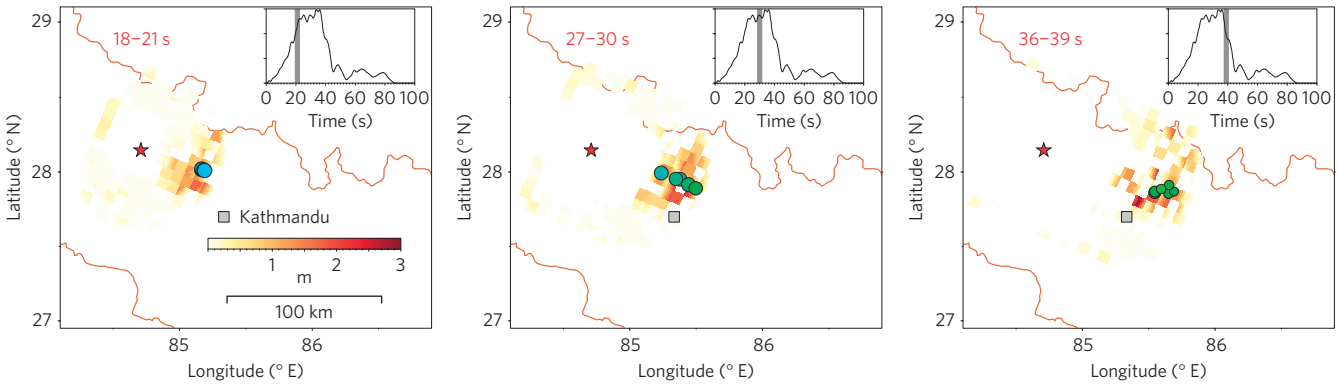

Figure 3 | Time snapshot of seismic rupture evolution. Each plot shows slip (shaded to colour scale) and high-frequency sources (dots, coloured by their rupture time, same scale as in Fig. 2) occurring within a 3 s window, indicated by a grey band over the source time function in the inset. The red star indicates the epicentre. An animation is provided in Supplementary Methods.

Both the back-projection results and the finite fault source model suggest that the earthquake unzipped the downdip edge of the locked zone, propagating mostly as a mode-III crack. The persistent radiation of high-frequency waves along the whole rupture length is probably due to the high and heterogeneous stresses built up at the transition between the locked and the creeping zone. The stress heterogeneities can result from intermingling of creeping and locked areas at a scale not resolvable with surface geodesy. Another factor contributing to stress heterogeneity is the background seismicity, which is well understood to be triggered by stress build-up at the downdip edge of the locked zone[5,15]. The correlation between the moment rate and the power of high-frequency seismic radiations suggests that the high-frequency sources are 'riding the wave' of an ongoing slip pulse. It is interesting to note that, although tremor-and-slip events are not directly comparable to standard earthquakes, a similar correlation has been observed during tectonic tremor episodes on subduction megathrusts[16]. The Gorkha earthquake actually shares similarities with earthquakes observed near the downdip end of the locked subduction megathrust[1] (zone C in ref. 17). In both settings, the high-frequency sources are found to radiate from the lower edge of the locked fault zone.

The rupture during the Gorkha earthquake expanded upwards from the locked edge, but not much downwards—probably because the zone of aseismic slip acted as an efficient barrier[4] to downdip propagation of the seismic rupture or because of the restraining effect of a ramp along the MHT (ref. 6). The pattern of coupling can thus explain the location of the earthquake initiation and the rupture process, but not its arrest along strike.

The rupture seems to have derailed from its linear along-strike propagation after ~45 s, close to the location of the 12 May M_w 7.3 aftershock, although the trend towards the Australian network suggests that it could reflect a 'swimming' artefact (mitigation of this artefact by the MUSIC technique is imperfect when the energy gets weak). In any case, the eastward rupture propagation was possibly arrested when it encountered some structural complexity, a zone of lower stress on the MHT due to past seismicity or a rate-strengthening patch, which could have inhibited the rupture propagation. Interestingly, the mainshock and the 12 May aftershock almost entirely ruptured a segment of persistently intense background seismicity seen over the past 20 years of local seismic monitoring. The rupture initiated clearly at the western end of this segment. Lateral variations of the background seismicity and of the pattern and intensity of high-frequency sources could reflect lateral ramps along the MHT (ref. 18).

The 2015 Gorkha earthquake is similar in location to the 1833 earthquake, with estimated magnitude M_w 7.6–7.7, which also caused heavy damages in Kathmandu[19,20]. These earthquakes clearly did not propagate to the front of the Himalaya where the MHT emerges at the surface. However, palaeoseismological studies have shown that several larger Himalayan earthquakes have reached the surface[21,22]. In particular, the 1934 Bihar–Nepal earthquake[23] ruptured the MHT east of Kathmandu (Fig. 1), producing over 6 m of slip at the surface and reaching an estimated magnitude of M_w 8.2 (ref. 24). Its rupture extent is weakly constrained but consistent with the possibility that the Gorkha earthquake sequence arrested because of the lower stress level left by the 1934 event or as a result of some local complexity of structural origin. A lateral ramp of the MHT, or an heterogeneity of fault friction—for example, a small patch with rate-strengthening friction not resolvable with the interseismic geodetic data—could have resulted in a barrier effect and a persistent segmentation of the MHT.

A previous large earthquake in 1255 also reached the surface[23,24]. The area east of Kathmandu seems unlikely to rupture again in the near future in a large (say $M_w > 7.5$) event. The 81-yr time span since 1934 is short in comparison to the 679-yr separation between 1255 and 1934 and the accumulated slip deficit since 1934 amounts to less than 2 m. The 1813 and 2015 earthquakes must have contributed to the process of upward transfer of the stresses which build up around the downdip edge of the locked fault zone in the interseismic period. This mechanism is observed in dynamic models of the seismic cycle, and ultimately leads to rupture of the whole locked zone[25]. It is also possible that the 2015 and 1833 earthquakes produced similar ruptures, but failed to rupture the locked portions of the MHT beneath and west of the Kathmandu basin because of some persistent barrier of mechanical or structural origin. Yet another possibility is that slip on the updip locked portion of the MHT is not entirely seismic. The stress increase could, in principle, be released by afterslip if the updip fault portion obeyed a rate-strengthening friction law and was previously lying in the stress shadow[26] of the asperity which ruptured in 2015. If so, it should be observed to slip aseismically in the post-seismic period.

The locked portion of the MHT west of the 2015 event calls for special attention, as the nearly 800-km-long stretch between the 1833/2015 ruptures and the 1905 M_w 7.8 Kangra earthquake is a well-identified seismic gap with no large earthquake for over 500 years[18,22,27]. The MHT is clearly locked there (Fig. 1) and its deficit of slip could exceed 10 m. The last large earthquake there occurred in 1505, and could have exceeded M_w 8.5 (ref. 28). This event produced significant damage in southern Tibet and ruptured the Himalayan foothills at the surface[29]. Although the size of that particular event is debated, there is general consensus that major earthquakes ($M_w > 8.5$) have occurred along that stretch of the Himalaya, and could have produced over 10 m of slip along the Himalayan front[18,22,27].

Methods

Methods and any associated references are available in the online version of the paper.

Received 13 May 2015; accepted 21 July 2015;
published online 6 August 2015

References

1. Schurr, B. *et al.* Gradual unlocking of plate boundary controlled initiation of the 2014 Iquique earthquake. *Nature* **512,** 299–302 (2014).
2. Loveless, J. P. & Meade, B. J. Spatial correlation of interseismic coupling and coseismic rupture extent of the 2011 $M_w = 9.0$ Tohoku-oki earthquake. *Geophys. Res. Lett.* **38,** L17306 (2011).
3. Yue, H. *et al.* The 5 September 2012 Nicoya, Costa Rica M_w 7.6 earthquake rupture process from joint inversion of high-rate GPS, strong-motion, and teleseismic P wave data and its relationship to adjacent plate boundary interface properties. *J. Geophys. Res.* **118,** 5453–5466 (2013).
4. Kaneko, Y., Avouac, J. P. & Lapusta, N. Towards inferring earthquake patterns from geodetic observations of interseismic coupling. *Nature Geosci.* **3,** 363–369 (2010).
5. Ader, T. *et al.* Convergence rate across the Nepal Himalaya and interseismic coupling on the Main Himalayan Thrust: Implications for seismic hazard. *J. Geophys. Res.* **117,** B04403 (2012).
6. Pandey, M. R., Tandukar, R. P., Avouac, J. P., Lave, J. & Massot, J. P. Interseismic strain accumulation on the Himalaya crustal ramp (Nepal). *Geophys. Res. Lett.* **22,** 751–754 (1995).
7. M7.8–36 km E of Khudi, Nepal. *USGS* (2015); http://earthquake.usgs.gov/earthquakes/eventpage/us20002926#general_summary
8. Lavé, J. & Avouac, J. P. Active folding of fluvial terraces across the Siwaliks Hills, Himalayas of central Nepal. *J. Geophys. Res.* **105,** 5735–5770 (2000).
9. M7.3–19 km SE of Kodari, Nepal. *USGS* (2015); http://earthquake.usgs.gov/earthquakes/eventpage/us20002ejl#general_summary
10. Nabelek, J. *et al.* Underplating in the Himalaya-Tibet collision zone revealed by the Hi-CLIMB Experiment. *Science* **325,** 1371–1374 (2009).
11. Lemonnier, C. *et al.* Electrical structure of the Himalaya of Central Nepal: High conductivity around the mid-crustal ramp along the MHT. *Geophys. Res. Lett.* **26,** 3261–3264 (1999).
12. Bilham, R. *et al.* GPS measurements of present-day convergence across the Nepal Himalaya. *Nature* **386,** 61–64 (1997).
13. Ishii, M., Shearer, P. M., Houston, H. & Vidale, J. E. Extent, duration and speed of the 2004 Sumatra-Andaman earthquake imaged by the Hi-Net array. *Nature* **435,** 933–936 (2005).
14. Ji, C., Wald, D. & Helmberger, D. V. Source Description of the 1999 Hector Mine, California Earthquake, Part I: Wavelet Domain Inversion Theory and Resolution Analysis. *Bull. Seismol. Soc. Am.* **92,** 1192–1207 (2002).
15. Cattin, R. & Avouac, J. P. Modeling mountain building and the seismic cycle in the Himalaya of Nepal. *J. Geophys. Res.* **105,** 13389–13407 (2000).
16. Ide, S., Imanishi, K., Yoshida, Y., Beroza, G. C. & Shelly, D. R. Bridging the gap between seismically and geodetically detected slow earthquakes. *Geophys. Res. Lett.* **35,** L10305 (2008).
17. Lay, T. *et al.* Depth-varying rupture properties of subduction zone megathrust faults. *J. Geophys. Res.* **117,** B04311 (2012).
18. Mugnier, J. L. *et al.* Structural interpretation of the great earthquakes of the last millennium in the central Himalaya. *Earth Sci. Rev.* **127,** 30–47 (2013).
19. Ambraseys, N. N. & Douglas, J. Magnitude calibration of north Indian earthquakes. *Geophys. J. Int.* **159,** 165–206 (2004).
20. Bilham, R. Location and magnitude of the 1833 Nepal earthquake and its relation to the rupture zones of contiguous great Himalayan earthquakes. *Curr. Sci.* **69,** 101–128 (1995).
21. Lavé, J. *et al.* Evidence for a great medieval earthquake (approximate to 1100 AD) in the Central Himalayas, Nepal. *Science* **307,** 1302–1305 (2005).
22. Kumar, S. *et al.* Paleoseismic evidence of great surface-rupture earthquakes along the Indian Himalaya. *J. Geophys. Res.* **111,** B03304 (2006).
23. Sapkota, S. N. *et al.* Primary surface ruptures of the great Himalayan earthquakes in 1934 and 1255. *Nature Geosci.* **6,** 71–76 (2013).
24. Bollinger, L. *et al.* Estimating the return times of great Himalayan earthquakes in eastern Nepal: Evidence from the Patu and Bardibas strands of the Main frontal thrust. *J. Geophys. Res.* **119,** 7123–7163 (2014).
25. Lapusta, N., Rice, J. R., Ben-Zion, Y. & Zheng, G. T. Elastodynamic analysis for slow tectonic loading with spontaneous rupture episodes on faults with rate- and state-dependent friction. *J. Geophys. Res.* **105,** 23765–23789 (2000).
26. Bürgmann, R. *et al.* Interseismic coupling and asperity distribution along the Kamchatka subduction zone. *J. Geophys. Res.* **110,** B07405 (2005).
27. Rajendran, C. P., John, B. & Rajendran, K. Medieval pulse of great earthquakes in the central Himalaya: Viewing past activities on the frontal thrust. *J. Geophys. Res.* **120,** 1623–1641 (2015).
28. Bilham, R. & Wallace, K. Future $M_w > 8$ earthquakes in the Himalaya: Implications from the 26 Dec 2004 $M_w = 9.0$ earthquake on India's eastern plate margin. *Geol. Surv. India* **85,** 1–14 (2005).
29. Yule, D., Dawson, S., Lave, J., Sapkota, S. & Tiwari, D. *AGU Fall Meeting* Abstract #S33C-05 (AGU, 2006).
30. Rajaure, S. *et al.* Pandey. Double difference relocation of local earthquakes in the Nepal Himalaya. *J. Nepal Geol. Soc.* **46,** 133–142 (2013).

Acknowledgements

Sentinel-1A data are provided by the European Space Agency. T.W. thanks J. Kim from SMU for help in processing the SAR data. We also thank R. Bürgmann for comments on an earlier version of this study. J.-Ph.A. thanks the BP Foundation and the Royal Society for support.

Author contributions

J.-Ph.A. coordinated the research and wrote the article. L.M. and J.-P.A. carried out the back-projection. S.W. carried out the finite source modelling. T.W. carried out the SAR offset measurements. All authors contributed to the interpretation and writing of the article.

Additional information

Supplementary information is available in the online version of the paper. Reprints and permissions information is available online at www.nature.com/reprints. Correspondence and requests for materials should be addressed to J.-Ph.A.

Competing financial interests

The authors declare no competing financial interests.

Methods

We describe here the methods used in this study. We have opted not to make the corresponding computer codes available online, as these are not user-friendly codes with manuals—however, they can be provided on request from the authors. The waveform data are available from the Incorporated Research Institutions for Seismology (IRIS) website (http://ds.iris.edu/ds/nodes/dmc/data/#requests).

Back-projection of high-frequency teleseismic seismic waveforms. The coseismic rupture process of the 2015 M_w 7.8 Gorkha earthquake is well imaged by the back-projection (BP) approach, which provides a high-frequency view of the rupture process. In contrast to classic source inversions based on waveform fitting, the approach does not require detailed knowledge of the Green's function and relies solely on the timing information of coherent seismograms. The BP approach is therefore less affected by any uncertainty in seismic velocity structures or the assumptions of fault geometry and rupture kinematics. The BP analysis is typically performed on coherent seismograms recorded at teleseismic distances. Here, we use the seismograms recorded by the Australian seismic network (AU), composed of 54 broadband stations evenly distributed across continental Australia with epicentral distances between 60° and 95° (Supplementary Fig. 1). The data of the AU network are available from the IRIS data centre. We band-pass-filtered the AU seismograms between 2 s and 0.5 s, the highest band with relatively high waveform coherency (Supplementary Fig. 2). We aligned the initial P-wave arrivals of the filtered waveforms with a multichannel cross-correlation technique[31]. The first arrival is assumed to come from the USGS hypocentre location (84.71° E, 28.15° N). The locations of the later high-frequency sources are determined based on the differential travel time relative to the hypocentre. As differential travel time is not sensitive to relatively small source depth changes along the shallow dipping MHT, we back-projected the waveforms onto a horizontal fault plane at a depth of 15 km, based on the IASP91 velocity model. We adopted the Multitaper-MUSIC array processing technique[32], which resolves more closely spaced sources and is less sensitive to aliasing, yielding a sharper image of the rupture process than the standard beamforming approach[33]. We also applied a 'reference window' strategy[34], which eliminates the 'swimming' artefacts, a systematic apparent drift of the high-frequency energy towards the station arrays.

SAR data and processing. We used two pairs (descending Path 19 and ascending Path 85) of Sentinel-1A Synthetic Aperture Radar (SAR) images from the European Space Agency to map the surface deformation caused by the earthquake. The radar images were acquired in the Terrain Observation by Progressive Scan (TOPS) mode, which is designed for carrying out routine, SAR-based observations[35]. We aligned the post-seismic image (acquired on 29 April and 3 May) along with the pre-seismic image (acquired on 9 and 17 April) using the GAMMA software[36], and then calculated the cross-correlation between uniformly distributed non-overlapping 64-by-64 sub-images on the co-registered radar amplitude images. The peak location in the obtained cross-correlation surface indicates the offset between the two sub-images in both azimuth (satellite travelling direction) and range (radar line-of-sight direction, LOS; refs 37,38).

Offsets between the SAR image pairs are attributed to the ground displacement as well as to imaging geometry differences and topography. We therefore calculated the geometric offsets from the orbital information and the Shuttle Radar Topography Mission Digital Elevation Model (SRTM DEM; ref. 38). After geometric correction, a low-frequency trend still exists in the offsets field, probably due to inaccurate orbital information. We removed this component by fitting a polynomial surface from the offsets located in the far field. The derived range offsets measure ground displacement in the LOS directions that are from 32 to 46 degrees from the vertical, with a component towards the west and east, whereas the azimuth offsets measures along-track components, which is about SSW (191° eastward from North) and NNW (11° westward from North) for the descending and ascending data, respectively. We used an initial slip model to generate two synthetic surface displacements in the radar LOS and azimuth directions. We used the predicted displacements to generate two quadtree sub-sampling grids[39], on which we extracted median values from offsets within each grid, resulting in 263 and 715 data points in azimuth and range, respectively, from the descending track P19, and 499 and 786 data points in azimuth and range, respectively, from the ascending track P85 (Supplementary Fig. 3). For each downsampled data point, we calculated the line-of-sight vector based on its geolocation and the satellite orbital information.

The accuracy of SAR image offsets depends on the cross-correlation peak, and can reach around 1/10–1/20 of the pixel spacing[40]. For the Sentinel-1A TOPS image, the azimuth and range pixel spacings are 14 m and 2.3 m respectively; as a consequence, azimuth offsets are useful only when the north–south component of the horizontal deformation is large, which is the case for the Gorkha earthquake. Range offsets measure the surface deformation in the same direction as interferometry, which can be formed from the same SAR image pair. However, the phase information is seriously decorrelated in the mountainous areas of the Himalaya. In addition, the high deformation gradient surrounding the peak deforming area may result in aliasing of the phase values. As both factors can cause unreliable phase unwrapping results, we decided to use image offsets data for our model inversion.

Finite source modelling and inversion procedure. We downloaded GSN broadband data from the IRIS DMC. We analysed 40 teleseismic P and 37 SH waveforms selected on the basis of data quality and azimuthal distribution. Waveforms are first converted to displacement by removing the instrument response in the frequency range lower than 1 Hz. The geodetic data were obtained by cross-correlation of sentinel-1 SAR data, both for ascending and descending images (see previous section for more details).

We approximate the fault geometry with a planar fault segment with a strike of 293° and a dip of 7° (GCMT), each discretized in 8×8 km^2 subfaults. The model assumes that the rupture consists of a propagating rupture front with slip accruing in the wake of the passage of the rupture front. The slip history at each grid point (j,k) on the fault is represented by $D \times \dot{S}_{jk}(t)$, where $\dot{S}_{jk}(t)$ is the slip-rate function, which specifies how a point on the fault slips in time, and D is the cumulative (or 'static') slip. The rise-time function is represented by a cosine function parameterized by the duration of slip—the so-called rise time. Because the seismograms are band-pass-filtered, this rather smooth slip-rate function is adopted, although a more abrupt slip-rate function would probably be more realistic[41]. For each subfault, we solve for the slip amplitude and rake, rise time and rupture velocity. The Green's functions are generated assuming a one-dimensional model derived from a local seismic network[42] (Supplementary Table 1).

The determination of a finite fault slip model is an underdetermined problem due to the large number of unknowns and numerous trade-offs among model parameters, such as rise time and rupture velocity. In the present case the trade-offs are significantly reduced if coseismic geodetic observations are available and inverted jointly with the seismological data. Even so, the determination of a finite fault source remains generally underdetermined if the fault discretization is too fine. One way to regularize the inversion is setting some constraints on the roughness of the slip distribution, which is the approach adopted here.

We define the best fit model as having the lowest objective function, given as:

$$\text{Misfit} = Ewf + WI * EI + WS * S + Ww * M$$

where Ewf is the waveform misfit, EI is the geodetic misfit, S is a normalized, second derivative of slip between adjacent patches (a so-called Laplacian smoothing), M is a normalized seismic moment, and WI, WS and Ww are the relative weights applied to the geodic misfit, smoothing and moment, respectively. The least squares misfits are calculated for the teleseismic and geodetic data. Here we tested different values of WI, and found that setting the weight for the geodetic misfits twice as large as for the waveform misfits did not significantly degrade the fits to the teleseismic or geodetic data between the individual and joint inversions, given the normalization schemes. The static Green's functions at the free surface are calculated by using the same one-dimensional velocity model (Supplementary Table 1) as used in teleseismic body-wave calculation. The fit to the P-waves is given twice as much weight as that to the SH-waves. There are two main reasons for this: it is much easier to select first arrivals of P-waves than those of SH-waves, owing to larger noise in the SH-waves; and SH-waves are usually more sensitive to the three-dimensional velocity structure. Thus, in general, SH-wave fits are not as good as P-wave fits—in particular for thrust events. Here the P-wave and geodetic data are the most robust and clean data, and thus provide the better constraints on the rupture process.

We use a simulated annealing algorithm[14] to find the best-fitting model parameters for the joint inversions for coseismic slip. This nonlinear, iterative inversion algorithm is designed to avoid local minima by searching broadly through parameter space in the initial steps, and then in later iterations focusing on regions that fit the data well.

We determined the best-fitting mean rupture velocity by imposing the constraint that the rupture velocity be constant. Supplementary Fig. 5 shows how the fit to the waveforms varies for rupture velocities between 1 and 4 km s^{-1}. The best-fitting value is 3.0 ± 0.5 km s^{-1}. We also performed an inversion with variable rupture velocity (Supplementary Fig. 6).

References

31. Vandecar, J. C. & Crosson, R. S. Determination of teleseismic relative phase arrival times using multi-channel cross-correlation and least-squares. *Bull. Seismol. Soc. Am.* **80,** 150–169 (1990).
32. Meng, L. S., Inbal, A. & Ampuero, J. P. A window into the complexity of the dynamic rupture of the 2011 M_w 9 Tohoku-Oki earthquake. *Geophys. Res. Lett.* **38,** L00G07 (2011).

33. Meng, L., Ampuero, J. P., Sladen, A. & Rendon, H. High-resolution backprojection at regional distance: Application to the Haiti M7.0 earthquake and comparisons with finite source studies. *J. Geophys. Res.* **117,** B04313 (2012).
34. Meng, L. S., Ampuero, J. P., Luo, Y. D., Wu, W. B. & Ni, S. D. Mitigating artifacts in back-projection source imaging with implications for frequency-dependent properties of the Tohoku-Oki earthquake. *Earth Planets Space* **64,** 1101–1109 (2012).
35. De Zan, F. & Guarnieri, A. M. TOPSAR: Terrain observation by progressive scans. *IEEE Trans. Geosci. Remote Sens.* **44,** 2352–2360 (2006).
36. Wegmuller, U. & Werner, C. in *Proc. Third ERS Symp. Space Service Environment* Vol. III, 1687–1692 (Special Publications 414, ESA, 1997).
37. Michel, R., Avouac, J. P. & Taboury, J. Measuring ground displacements from SAR amplitude images: Application to the Landers earthquake. *Geophys. Res. Lett.* **26,** 875–878 (1999).
38. Wang, T., Jonsson, S. & Hanssen, R. F. Improved SAR Image Coregistration Using Pixel-Offset Series. *IEEE Geosci. Remote Sens. Lett.* **11,** 1465–1469 (2014).
39. Jonsson, S., Zebker, H., Segall, P. & Amelung, F. Fault slip distribution of the 1999 Mw 7.1 Hector Mine, California, earthquake, estimated from satellite radar and GPS measurements. *Bull. Seismol. Soc. Am.* **92,** 1377–1389 (2002).
40. Bamler, R. & Eineder, M. Accuracy of differential shift estimation by correlation and split-bandwidth interferometry for wideband and Delta-k SAR systems. *IEEE Geosci. Remote Sens. Lett.* **2,** 151–155 (2005).
41. Tinti, E., Bizzarri, A. & Cocco, M. Modeling the dynamic rupture propagation on heterogeneous faults with rate- and state-dependent friction. *Ann. Geophys.* **48,** 327–345 (2005).
42. Mahesh, P. *et al.* One-dimensional reference velocity model and precise locations of earthquake hypocenters in the Kumaon-Garhwal Himalaya. *Bull. Seismol. Soc. Am.* **103,** 328–339 (2013).